Eur. J. Mineral., 35, 171–187, 2023
https://doi.org/10.5194/ejm-35-171-2023


European Journal of Mineralogy
Open Access

# Pervasive carbonation of peridotite to listvenite (Semail Ophiolite, Sultanate of Oman): clues from iron partitioning and chemical zoning

**Thierry Decrausaz[1], Marguerite Godard[1], Manuel D. Menzel[2,3], Fleurice Parat[1], Emilien Oliot[1], Romain Lafay[1], and Fabrice Barou[1]**

[1]Géosciences Montpellier, Université de Montpellier, CNRS, Montpellier, 34095, France
[2]Tectonics and Geodynamics, RWTH Aachen University, 52056 Aachen, Germany
[3]Petrology, Geochemistry and Geochronology (PGG), Instituto Andaluz de Ciencias de la Tierra (IACT), CSIC–UGR, Armilla, 18100, Spain

**Correspondence:** Thierry Decrausaz (thierry.decrausaz@umontpellier.fr)

Received: 17 June 2022 – Revised: 21 December 2022 – Accepted: 26 December 2022 – Published: 21 March 2023

**Abstract.** Earth's long-term cycling of carbon is regulated from mid-ocean ridges to convergent plate boundaries by mass transfers involving mantle rocks. Here we examine the conversion of peridotite to listvenite (magnesite + quartz rock) during $CO_2$ metasomatism along the basal thrust of the Semail Ophiolite (Fanja, Sultanate of Oman). At the outcrop scale, this transformation defines reaction zones, from serpentinized peridotites to carbonated serpentinites and listvenites. Based on a detailed petrological and chemical study, we show that carbonation progressed through three main stages involving the development of replacive textures ascribed to early stages, whilst carbonate (± quartz) veining becomes predominant in the last stage. The pervasive replacement of serpentine by magnesite is characterized by the formation of spheroids, among which two types are identified based on the composition of their core regions: Fe-core and Mg-core spheroids. Fe zoning is a type feature of matrix and vein magnesite formed during the onset carbonation (Stage 1). While Fe-rich magnesite is predicted to form at low fluid $XCO_2$ from a poorly to moderately oxidized protolith, our study evidences that the local non-redox destabilization of Fe oxides into Fe-rich magnesite is essential to the development of Fe-core spheroids. The formation of Fe-core spheroids is followed by the pervasive (over-)growth of Mg-rich spheroids and aggregates (Stage 2) at near-equilibrium conditions in response to increasing fluid $XCO_2$. Furthermore, the compositions of carbonates indicate that most siderophile transition elements released by the dissolution of primary minerals are locally trapped in carbonate and oxides during matrix carbonation, while elements with a chalcophile affinity are the most likely to be leached out of reaction zones.

## 1 Introduction

The (de-)serpentinization and (de-)carbonation of peridotites play a major role in the long-term cycling of volatiles, incompatible and fluid-mobile elements between the surface and the deep Earth (e.g., Alt et al., 2013; Deschamps et al., 2013; Kelemen and Manning, 2015). The carbonation of peridotites takes place in various hydrothermal systems, from seafloor exposure to convergent plate boundaries (e.g., Schwarzenbach et al., 2013; Schröder et al., 2015; Debret et al., 2018; Noël et al., 2018; Cannaò et al., 2020) or during (sub-)surface weathering (e.g., Kelemen and Matter, 2008; Ulrich et al., 2014). Listvenites represent the most extreme product of this metasomatic process, with the complete conversion of the primary and secondary silicates composing the peridotites (olivine, orthopyroxene – Opx, clinopyroxene – Cpx, serpentine) into a quartz–carbonate (magnesite ± dolomite) assemblage (Halls and Zhao, 1995). Listvenites and related carbonated serpentinites are found in several orogenic and ophiolitic peridotite massifs worldwide, typically along tectonic discontinuities acting as conduits for $CO_2$-rich metasomatic fluids (e.g., Hansen et al., 2005; Beinlich et al., 2012; Aftabi

and Zarrinkoub, 2013; Hinsken et al., 2017; Qiu and Zhu, 2018; Menzel et al., 2018; Boskabadi et al., 2020). Listvenites are well-known for hosting ore-grade mineralizations of economically valuable metals (e.g., transition elements such as Au, Ag, Co or Cu; e.g., Buisson and Leblanc, 1987; Auclair, 1993; Aftabi and Zarrinkoub, 2013; Emam and Zoheir, 2013; Belogub et al., 2017; Gahlan et al., 2020).

Over the years, the reaction pathways and mechanisms leading to complete peridotite carbonation have been investigated (e.g., Hansen et al., 2005; Tominaga et al., 2017; Menzel et al., 2018). The dissolution of precursor silicates and redox evolution in response to infiltration of $CO_2$-rich fluids have been hypothesized as major processes driving elemental remobilization during carbonation (e.g., Buisson and Leblanc, 1987; Auclair et al., 1993). The destabilization of Fe oxides during carbonation was also identified in a few listvenite suites (Tominaga et al., 2017; Menzel et al., 2018; Qiu and Zhu, 2018; Austrheim et al., 2021), supporting a possible impact of carbonation on local redox conditions (e.g., Frost, 1985). The redistribution of Fe and transition elements in carbonates during these processes remains however little documented.

We present a study of listvenites from the Fanja region in the Semail Ophiolite (Oman), where extensive outcrops are described (Glennie et al., 1974; Stanger, 1985; Wilde et al., 2002; Nasir et al., 2007; Falk and Kelemen, 2015; Boudier and Nicolas, 2018) and where Hole BT1B was drilled during the Oman Drilling Project (OmanDP; Kelemen et al., 2020). We document the relationships between the Fanja listvenites, serpentinized peridotites and adjacent lithologies in the field and downhole, with a focus on rock textures, microstructures and mineral compositions. Taking advantage of the unmatched density and quality of BT1B cores, we characterize the carbonation sequence leading to the pervasive replacement of serpentinized peridotites by carbonates, with an emphasis on matrix replacement textures and Fe redistribution at the onset of the sequence. We also discuss the impact of carbonation on the remobilization of Fe and transition elements and the role of the linkages between fluid flow and changes in redox and chemical compositions in these processes.

## 2 Geological setting and sampling

### 2.1 The Semail Ophiolite and outcropping listvenites

The Semail Ophiolite is a segment of Tethyan oceanic lithosphere obducted on the Arabian continental margin during the Upper Cretaceous (e.g., Coleman, 1981; Nicolas et al., 2000) (Fig. 1a). It preserves a thick mantle section overlain by a layered oceanic crust, comprising lower-layered gabbros to upper volcanics. The mantle section is composed of moderately to highly serpentinized harzburgites and minor dunites, with Cpx–harzburgites and lherzolites toward the base of the section (Lippard et al., 1986; Godard et al., 2000; Takazawa et al., 2003; Boudier et al., 2010; Hanghøj et al., 2010). A 50–200 m thick section of highly serpentinized, mylonitized and often amphibole-bearing Cpx-rich peridotites alternating with dunites and minor harzburgites characterizes the transition of the ophiolite to underlying lithologies (e.g., Khedr et al., 2013; Prigent et al., 2018). A 10–100 m thick metamorphic sole outcrops discontinuously along the base of the ophiolite (e.g., Soret et al., 2017); it is made up of slivers of mafic and sedimentary-derived material. It records peak metamorphism in amphibolite to granulite facies ascribed to intra-oceanic underthrusting (e.g., Boudier et al., 1988) or incipient subduction (e.g., Searle and Cox, 1999). Zircon dating indicates that the formation of the sole was in part contemporaneous to the accretion of the oceanic crust preserved by the ophiolite (96.1–95.2 Ma; Rioux et al., 2021). During obduction, the ophiolite and metamorphic sole were thrust over the allochthonous Hawasina units comprising the relicts of a wide oceanic basin (volcanics, pelagic and shelf sediments; e.g., Bechennec et al., 1990) and onto the autochthonous Arabian basement rocks. Ophiolite obduction was followed by burial and then by an extensional phase of exhumation forming the Jebel Akhdar and Saih Hatat domes (Garber et al., 2021).

Listvenites crop out discontinuously along the ophiolite basal thrust (Fig. 1a–b). They occur as decametric thick layers and lenses within serpentinite oriented parallel to the basal thrust or as blocks within tectonic mélanges in shear zones (Nasir et al., 2007). The best-exposed outcrops of listvenites are observed in the Fanja region where the ophiolite section is relatively thin (Boudier and Nicolas, 2018). It exposes dismembered and highly faulted fragments of mantle peridotites, juxtaposed with lower gabbros and slices of metamorphic sole (Fig. 1b). The Fanja listvenites are aligned along a northwest–southeast direction to the north and to the south of the ophiolite segments flanking the Jebel Akhdar and Saih Hatat domes. The petrologic and thermometry studies of the listvenites indicate that carbonation occurred below 250 °C during cooling (Kelemen et al., 2022; Falk and Kelemen, 2015), with temperatures ranging from $247 \pm 52$ to $45 \pm 5$ °C for BT1B cores (Beinlich et al., 2020). The depth of formation of listvenites is however poorly constrained: it is less than 40 km assuming a subduction zone setting (Kelemen et al., 2022) and $\sim$ 3.75–7.5 km for geothermal gradients expected during obduction (Beinlich et al., 2020).

Fieldwork and sampling of serpentinized peridotites, carbonated serpentinites and listvenites was realized at three sites (Fig. 1b), along transects from the metamorphic sole to the overlying gabbros (Figs. 2 and S1): OmanDP Hole BT1B, Site 1 in Wadi Mansah (southern alignment of listvenites) and Site 2 in the Jebel Fanja (northern alignment of listvenites).

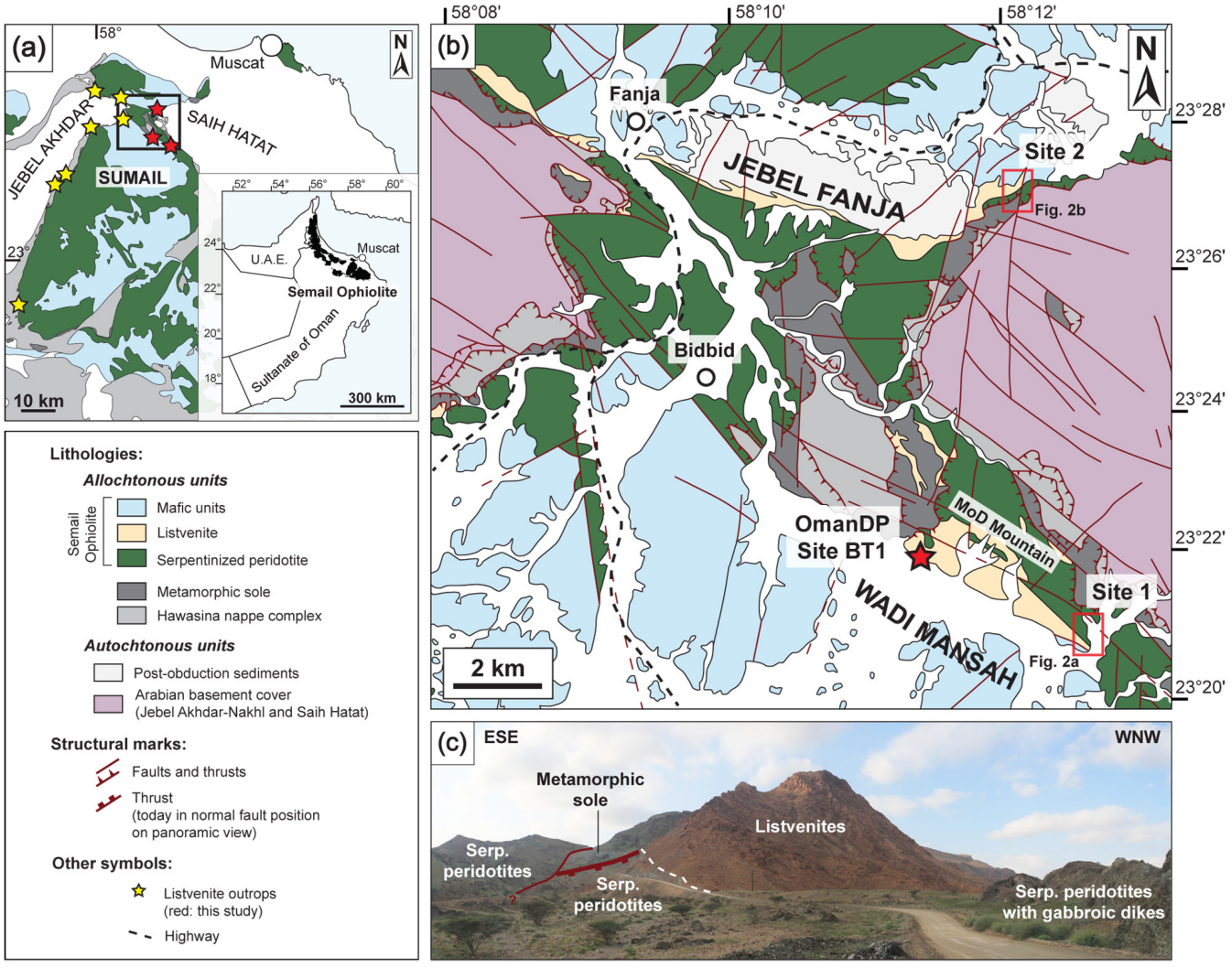


**Figure 1.** Listvenite outcrops in the Fanja area (Semail Ophiolite). **(a)** Location of the Semail Ophiolite in insert (based on Nicolas et al., 2000) and Sumail massif. Listvenite occurrences (yellow stars) are reported from Nasir et al. (2007) and Boudier and Nicolas (2018). **(b)** Geological map of the Fanja area (modified from Villey et al., 1986; Kelemen et al., 2022), indicated by a black rectangle in the insert map in **(a)**. **(c)** Field photograph of a lithological contact between listvenites and serpentinized peridotites at Site 2 (Jebel Fanja; PV in Fig. 2b).

## 2.2 Sampling

### 2.2.1 OmanDP Hole BT1B

Hole BT1B recovered ∼ 200 m of listvenites interlayered by two levels of carbonated serpentinites atop ∼ 100 m of metamorphic rocks (Kelemen et al., 2020; Fig. S1). Petrographic studies and bulk rock geochemical analyses of the mantle-derived section revealed three chemically distinct domains indicating that the protolith comprised serpentinized harzburgites/dunites and lherzolites as commonly observed along the ophiolite basal thrust (Godard et al., 2021). Listvenites are composed dominantly of magnesite and quartz forming the rock matrix along with minor dolomite and fuchsite (Cr-bearing muscovite), as well as accessory (relict) Cr-spinel, hematite and Fe hydroxides. Fuchsite is observed only in listvenites from the lherzolitic protolith domain. Listvenites and carbonated serpentinites are cut by numerous generations of different carbonate and quartz veins (Kelemen et al., 2020; Menzel et al., 2022) and cataclasites (Menzel et al., 2020). From Hole BT1B, 15 listvenites, 5 fuchsite-bearing listvenites and 9 carbonated serpentinites were selected for this study (Fig. S1, Tables S1–S2).

### 2.2.2 Site 1 and Site 2

Site 1 is located in the southeastern part of Wadi Mansah, ∼ 4.5 km east from Hole BT1B (Figs. 2 and S2). The mantle section (>250 m) is composed of massive serpentinized harzburgites and rare dunites. Listvenites are found atop the metamorphic sole to the north and interlayering peridotites

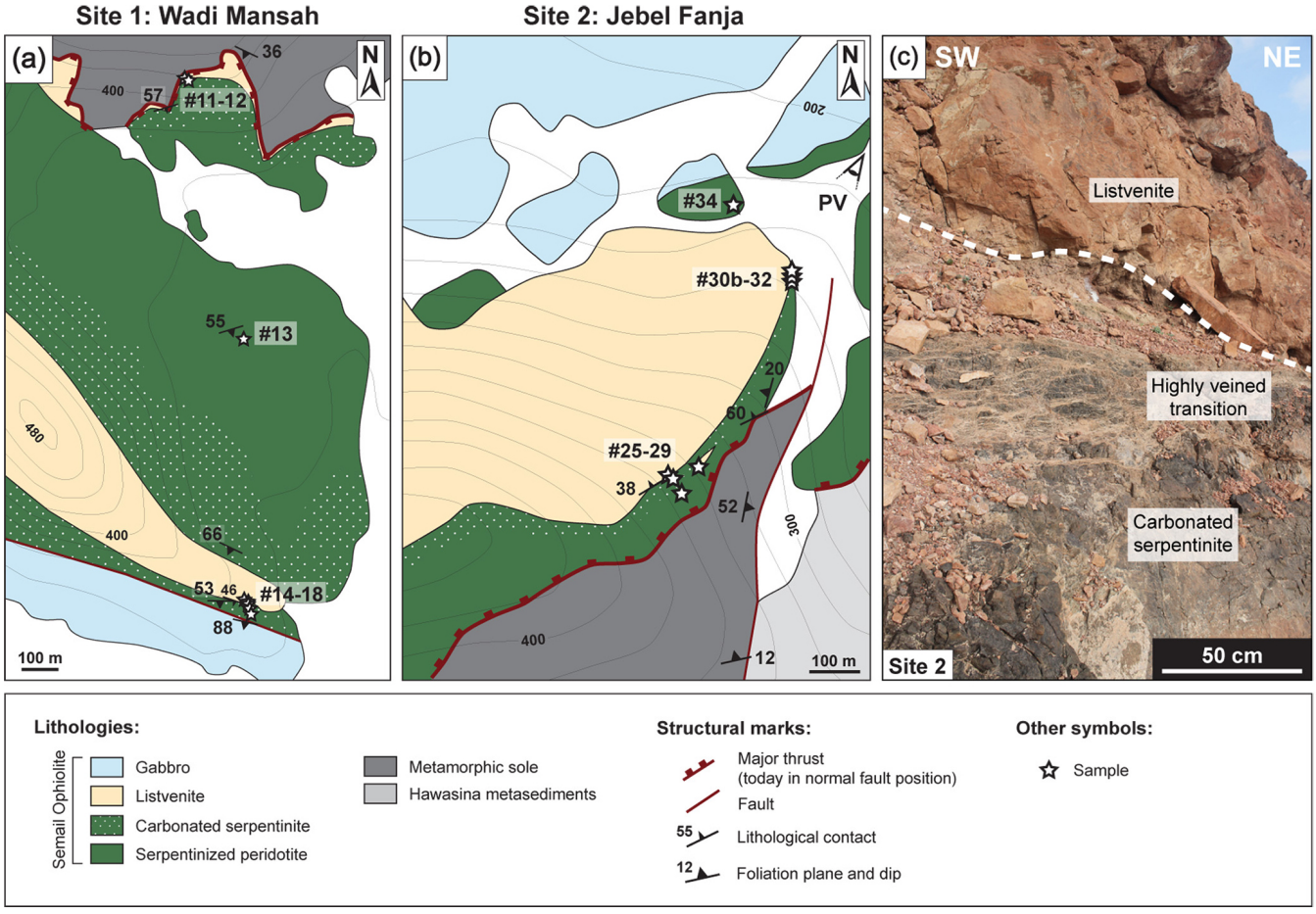


**Figure 2. (a–b)** Detailed geological maps of Site 1 (Wadi Mansah) and Site 2 (Jebel Fanja). Maps were drawn based on Villey et al. (1986) and field observations (this study, see Sect. 1 in Text S1). The topography was drawn from Google Earth maps. Location of samples is indicated by white stars; adjacent numbers refers to sample names. **(c)** Field photograph illustrating the mesoscale transition between listvenite and carbonated serpentinite at Site 2.

close to gabbros to the south. Lithological boundaries dip to the south-southwest and, except for the listvenite–peridotite interlayering, all contacts are faulted. Listvenites are orange-red due to weathering. The sole comprises, from top to bottom, mafic-derived rocks and metasediments. Listvenites in contact with the basal thrust form a 2–10 m thick layer below ∼ 20 m of foliated and fractured carbonated serpentinites. In the southern part, listvenites form a 10–50 m thick interval bordered by foliated and fractured carbonated serpentinites 5–10 m from the faulted contact with foliated gabbros. Listvenites are massive and host discontinuous millimetric to centimetric quartz–carbonate veins oriented at a high angle with the lithological contact. Fault contacts between listvenites, serpentinites and gabbros are highly variable, ranging from serpentinite fault gouge to foliated serpentinite with sharp localized faults. Close to gabbros, carbonated serpentinites host scarce gabbroic dikelets (< 10 cm thick) or pods. Away from gabbros, ∼ 25–50 m of deformed serpentinites show extensive matrix replacement by carbonates. Sampling includes one serpentinized harzburgite, four carbonated serpentinites and three listvenites (Fig. S1, Tables S1–S2).

Site 2 is located in the northeastern part of the Jebel Fanja, 9.5 km north from Hole BT1B (Figs. 2 and S2). This area exposes a ∼ 150 m thick mantle section comprising serpentinized harzburgites, interlayered by orange-red-stained listvenites to the north, close to overlying gabbros. Lithological boundaries dip to the north-northwest. Serpentinized harzburgites (∼ 100 m thick), often foliated and fractured, overlie the metamorphic sole. The sole comprises mafic-derived schists, with amphibolites locally along the basal thrust atop metasediments. Listvenites are found as a ∼ 50–75 m thick continuous planar structural level close to gabbros, draping the ridge and southern flank of the Jebel Fanja, and as plurimetric lenses within carbonated serpentinites. Listvenites are massive and crosscut by closely spaced submillimetric orange-red magnesite veins and by millimetric white quartz–carbonate veins, all oriented perpendicular to the contact with the underlying carbonated serpentinites

(∼ 3–20 m). Carbonated serpentinites are often foliated at the contact with listvenites and host millimetric to centimetric light orange magnesite veins, oriented at a low angle with the contact (Fig. 1c). Vein density increases towards listvenites. Rare millimetric red magnesite veins cut through both listvenites and carbonated serpentinites. Listvenites are overlain by serpentinized peridotites (>20 m) cross-cut by numerous gabbroic dikes and pods in proximity to gabbros. Sampling includes two serpentinized harzburgites, three carbonated serpentinites and three listvenites collected along two transects (Fig. S1, Tables S1–S2).

## 3 Petrographic, analytical and modeling methods

The petrography, microstructure and composition of carbonated serpentinites and listvenites were determined and mapped using optical microscopy and a CamScan Crystal Probe X500FE scanning electron microscope (SEM) equipped with an Ultim Max 100 EDS (energy-dispersive X-ray spectroscopy; SEM-EDS) detector at the Géosciences Montpellier SEM-EBSD facility. EDS data were processed with Oxford Instruments' AZtec. Further backscattered and secondary electron images were acquired using a Zeiss Gemini SUPRA 55 field-emission scanning electron microscope (FE-SEM) at the Institute of Tectonics and Geodynamics of RWTH Aachen University.

Mineral compositions of carbonates, silicates (serpentine, fuchsite), oxides and sulfides were quantified and mapped for a subset of 25 samples using a Cameca SX100 (Géosciences Montpellier) and a JEOL JXA-8530F HyperProbe (ISTE, University of Lausanne) electron probe microanalyzer (EPMA). Elemental maps were quantified by coupling EDS semi-quantitative data and EPMA compositions using XMapTools 3.4.1 MATLAB toolbox (Lanari et al., 2019). Transition elements were measured in carbonates and silicates for a subset of 12 samples by laser ablation inductively coupled plasma mass spectrometry (LA-ICP-MS) on a Thermo Scientific Element XR mass spectrometer (ISTE) and a Thermo Scientific Element 2 mass spectrometer (Géosciences Montpellier). Data were processed using Glitter (Griffin et al., 2008). Sample preparation, operating conditions, and analytical and data processing protocols are reported in Sect. 2 in Text S1. Analytical errors and measurements on reference materials are provided in Tables S3 and S9.

Thermodynamic calculations were performed using Perple_X 6.9.1 (Connolly, 2005, 2009), in a $H_2O$–$CO_2$ saturated FeO–$Fe_2O_3$–MgO–$SiO_2$ (FMS) system to constrain the stability fields of metasomatic assemblages resulting from carbonation at different redox budgets. The calculations were performed using the TC-DS622 version of the Holland and Powell (2011) thermodynamic database with equations of state for $H_2O$ and $CO_2$ based on Pitzer and Sterner (1995). Solid solution models were applied for magnesite–siderite (Holland and Powell, 1998), antigorite (Padrón-Navarta et al., 2013) and ideal solution models for talc and brucite. Hematite, magnetite and quartz were considered pure phases.

## 4 Results

### 4.1 Textural, microstructural and geochemical study of the carbonation sequence

Based on mineral replacement textures and cross-cutting vein relationships, we identified three main groups of carbonates corresponding to different stages of carbonation during the conversion of serpentinized peridotite to listvenite (Table 1 in the Supplement; this study; Kelemen et al., 2020; Beinlich et al., 2020; Menzel et al., 2022).

#### 4.1.1 Protolith

Relics of the mantle protolith were preserved at Sites 1 and 2. They comprise moderately to fully serpentinized porphyroclastic harzburgites (Fig. S3). Serpentinized harzburgites show a typical mesh texture locally cut by millimetric crack-seal chrysotile veins. Olivine appears as mesh cores rimmed by lizardite/chrysotile and magnetite strings. Opx shows static replacement to bastite along fractures and cleavages. Minor Cpx occurs at the rim of or in close proximity to Opx. The Cr-spinel is often thinly rimmed by magnetite or ferri-chromite. Olivine and pyroxenes are fully serpentinized at the transition with listvenite. Bastites and serpentines display overlapping compositions in most transition elements, serpentine veins having the lowest values (see Tables S4, S10 and S11). Bastites are distinguished from serpentine by their high Sc and Ti concentrations, similarly to their respective mineral precursors, pyroxene and olivine. Sulfides are rare. They are identified as Fe–Ni–Co-bearing by SEM-EDS in serpentinized harzburgite OM20-13 and as polydymite, a weathering product of pentlandite, in carbonated serpentinite 44Z-4-0-5.

#### 4.1.2 Stage 1: onset of carbonation

Stage 1 carbonates are identified in carbonated serpentinites and in listvenites.

The earliest occurrences of carbonates are pseudomorphic replacements of serpentine mesh and crack-seal veins by magnesite and, in rare samples, by dolomite (Menzel et al., 2022). Pseudomorphic magnesite has $XMg > 0.85$ (XMg: molar Mg / (Mg + Fe)) except when growing near to or at the expense of magnetite along the mesh ($XMg < 0.85$) (Fig. 3a). They are depleted in most transition elements compared to Semail Ophiolite mantle values, except for Mn and Zn (Fig. 6).

Antitaxial magnesite veins are the most abundant veins formed in Stage 1. They crosscut serpentinites and commonly form anastomosing or closely spaced vein networks.

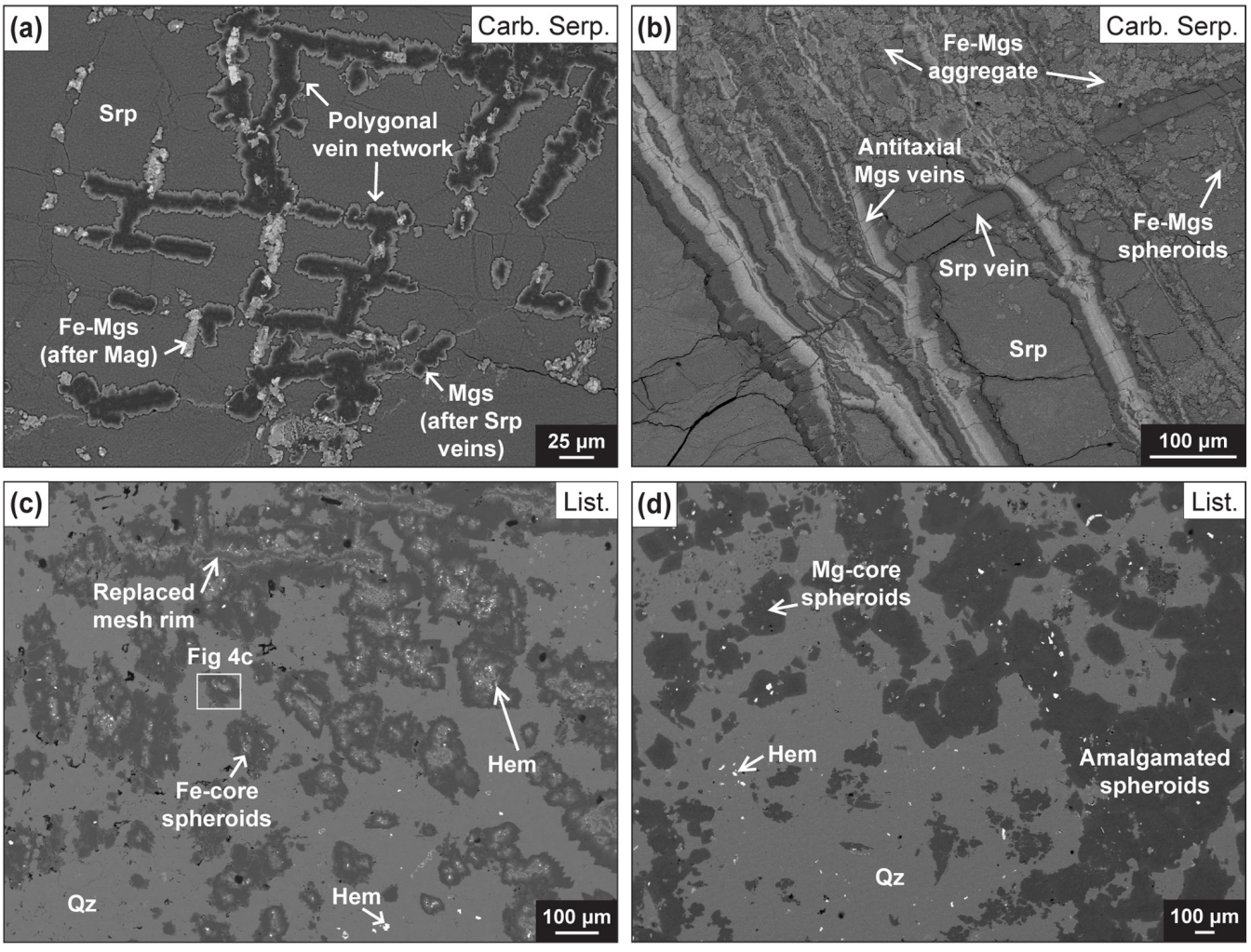


**Figure 3.** Backscattered electron (BSE) images of carbonate microstructures and textures representative of reaction Stage 1 **(a–c)** and Stage 2 **(d)**. **(a)** Magnesite replacing serpentine mesh rims in characteristic polygonal vein networks in carbonated serpentinite 44Z-2-47-50. **(b)** Crack-seal serpentine vein cut by antitaxial magnesite veins showing an Fe-rich median zone (light grey) and Mg-rich vein walls (dark grey) in carbonated serpentinite 44Z-4-0-5. Fe-rich magnesite spheroids and aggregates formed in the vicinity of antitaxial veins. **(c)** Fe-core spheroids (light grey cores) that developed in the vicinity of a former mesh rim preserved in listvenite 50Z-1-75-80. **(d)** Mg-core spheroids locally amalgamated to form aggregates in listvenite 46Z-4-46-51. Abbreviations: Hem: hematite; Mag: magnetite; Mgs: magnesite; Qz: quartz; Srp: serpentine.

They are characterized by chemical zoning with an Fe-rich median zone (XMg: 0.57–0.87) and Mg-rich edges (XMg: 0.89–0.97) (Fig. 3b). They are locally cut by cross-fiber to blocky unzoned magnesite veins (XMg: 0.93–0.97). They have transition element compositions comparable to those of pseudomorphic magnesite (Fig. 6).

Pervasive matrix carbonates occur as (a) isolated or grouped spheroidal magnesites presenting core-to-rim chemical zoning, defined as "spheroids" by Beinlich et al. (2020), and (b) aggregates formed by clustering spheroids or pervasive growth rooting from vein walls into the matrix (Figs. 3b, S3, S4). Magnesite spheroids have Fe-rich cores overgrown by Mg-rich magnesite (Figs. 5a, S5 and S6a–b); this magnesite zoning pattern is referred to in the following as Fe-core spheroids. Chemical mapping (Fig. 5a) indicates proportions of $\sim 19$ % and $\sim 81$ % for Fe-rich and Mg-rich magnesite respectively (Table S12). Fe-core spheroids are commonly $<100$ µm. They occur in the vicinity of mesh rims and zoned antitaxial veins, in domains with a low vein density. They are distinguished by the common presence of tiny inclusions of hematite (typical size: $<5$ µm) and characteristic destabilization textures around Fe oxides (Fig. 4a and c). In carbonated serpentinite OM20-26, such a destabilization texture shows microporosity at the carbonate–oxide interface (Fig. 4a). Fe-core spheroids have high concentrations of transition elements compared to other Stage 1 carbonates,

sometimes higher than Semail mantle values for Sc, Mn and Co (Figs. 6 and S6d).

#### 4.1.3 Stage 2: widespread replacement by Mg-rich magnesite and quartz

This stage is observed in listvenites but rarely in carbonated serpentinites; it is characterized by the complete replacement of serpentine by abundant Mg-rich magnesite and fine-grained background quartz. Chemical mapping (Fig. 5b and d) typically shows a high proportion of carbonates (~ 60 % of volume) compared to quartz (~ 34 % of volume) (see Table S12).

Magnesite occurs mainly as spheroids, aggregates and overgrowth on pre-existing microstructures. Magnesite spheroids have Mg-rich cores (mean XMg: ~ 0.96) and are referred to as Mg-core spheroids. They range in size between 50–300 µm (Fig. 3d) and show chemical zoning with Si and Fe enrichment toward the rims as illustrated on Mg# and Si/Mg maps in Fig. 5b and d. High-resolution mapping of the largest Mg-core spheroids reveals, in the outer regions, (a) Si–Ca-rich domains incorporating nano-inclusions of quartz (Fig. S6j) and (b) the development of Mg–Fe zoning patterns and the formation of high-Fe dendritic magnesites at the rims (Fig. S6g). Mg-rich magnesite aggregates (XMg = ~ 0.96) are composed of amalgamated Mg-core spheroids or by sub-millimetric subhedral to euhedral crystals. Mg-core spheroids and Mg-rich magnesite aggregates overlap in compositions for transition elements; they are both depleted compared to Fe-core spheroids (Figs. 6 and S6f–j). All carbonation textures are crosscut by cryptic quartz veins indicative of local silica remobilization (Menzel et al., 2022).

Anhedral to flaky hematite (~ 5–20 µm) occurs within the magnesite–quartz matrix, rimming altered Cr-spinel and replacing magnetite. Fuchsite is observed in a few core samples growing at the expense of Cr-spinel (e.g., listvenite 68Z-1-60-64) or intergrown with quartz in domains resembling bastite (e.g., listvenite 53Z-2-72-77). Textures point to fuchsite growth occurring concurrently with Stage 2 carbonates. Sulfides in listvenites are extremely rare, consisting of pyrite overgrown by magnesite (e.g., listvenite 46Z-4-46-51), polydymite, chalcocite and gersdorffite (e.g., listvenite 46Z-2-19-24).

#### 4.1.4 Stage 3: late generation of quartz and carbonate veins

Stage 3 is dominated by the formation of carbonate veins (mainly dolomite) and late cataclasis. Millimetric polycrystalline syntaxial carbonate–quartz and carbonate veins crosscut all pre-existing microstructures. Minor dolomite aggregates are also observed. Cataclasites reworking clasts of listvenite are locally cut or are cut by late dolomite veins. Carbonates have transition element compositions that are

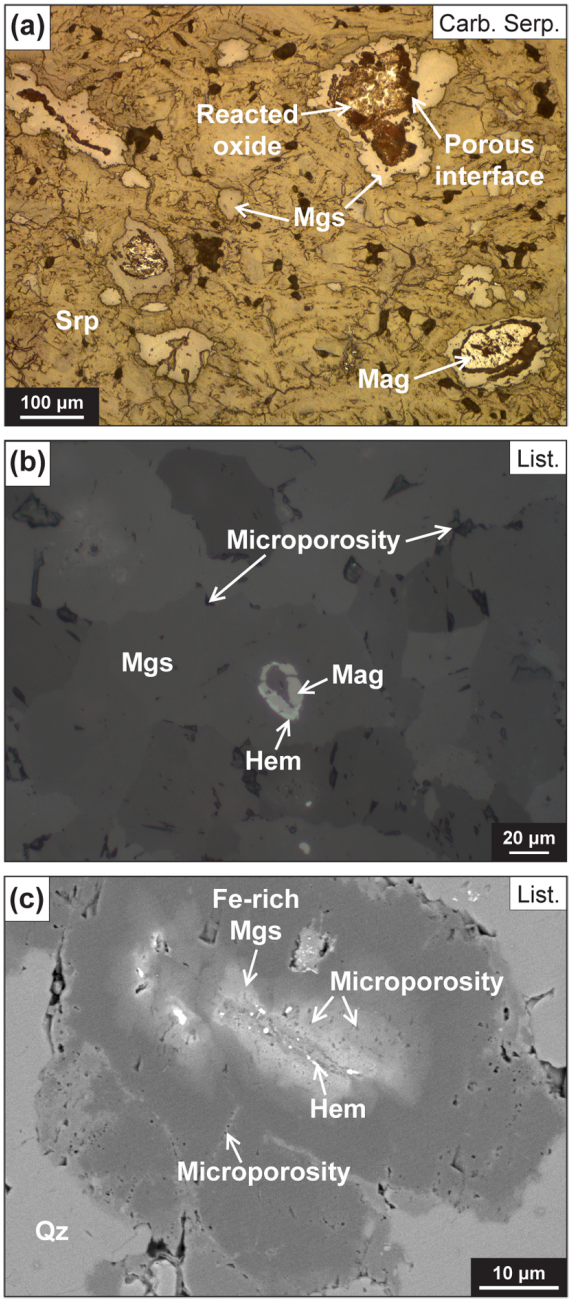


**Figure 4.** Textural relationships between Fe oxides and magnesite. **(a)** Reflected light (RL) image of spheroids in carbonated serpentinite OM20-26. Magnesite surrounding variously reacted Fe oxides ("reacted oxide") and magnetite. A porous interface connects oxide relicts and magnesite. **(b)** Magnetite destabilized into hematite and overgrown by magnesite aggregate in listvenite 71Z-2-21-26. Presence of a microporosity along (sub-)grain boundaries. **(c)** Internal Fe zoning of Fe-core spheroid, with hematite and a microporous zone outlining the relict of reacted Fe oxide. Abbreviations: Hem: hematite; Mag: magnetite; Mgs: magnesite; Qz: quartz; Srp: serpentine.

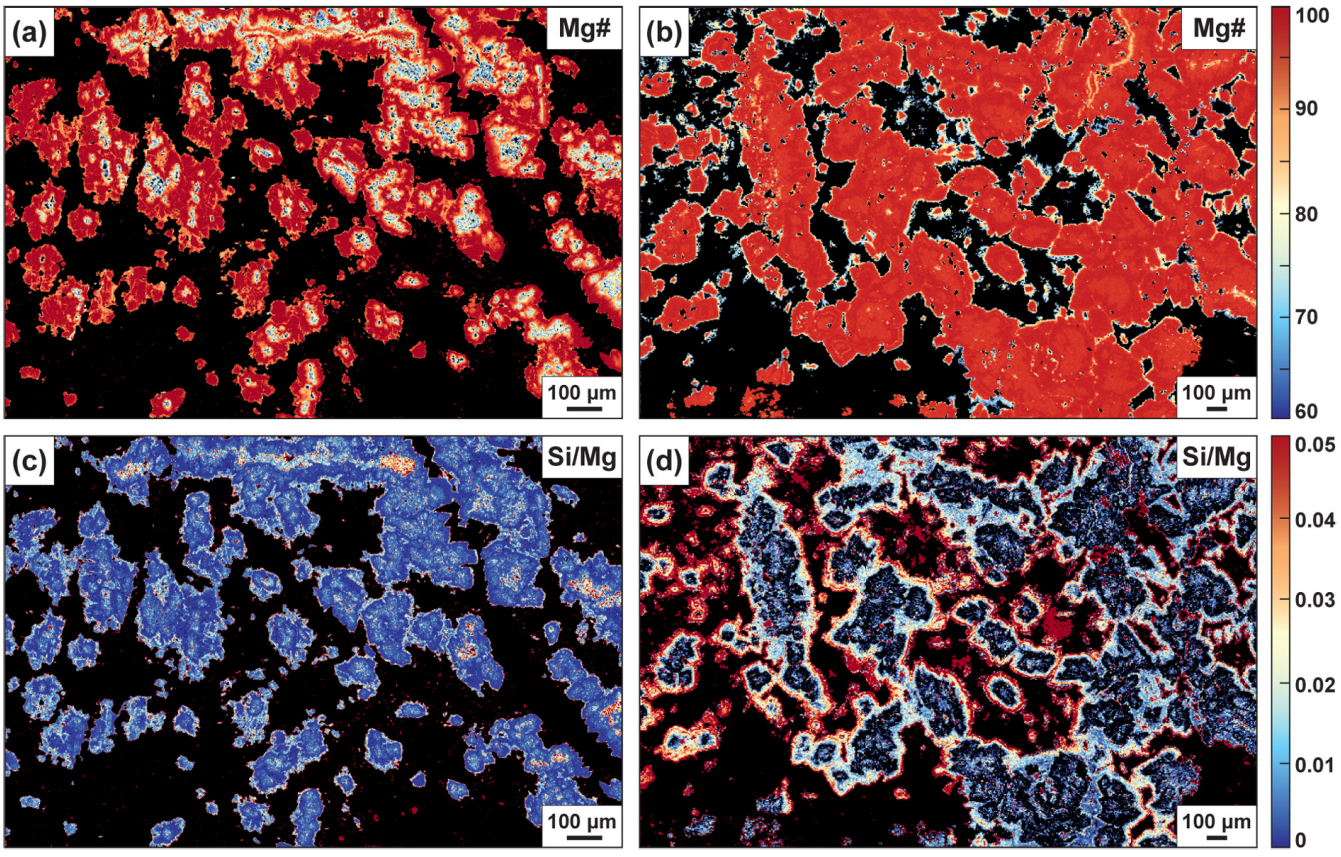


**Figure 5.** Quantitative Mg# and Si/Mg distribution maps of Fe-core (**a** and **c**, 50Z-01-75-80) and Mg-core spheroids (**b** and **d**, 46Z-4-46-51) in listvenites presented in Fig. 3c–d.

overall similar to Stage 1 and Stage 2 Mg-rich magnesite aggregates and veins (Fig. 6).

### 4.2 Thermodynamic modeling

Thermodynamic modeling is used to characterize the effects of variable $CO_2$ concentrations in fluids and redox conditions on mineral assemblages during carbonation at equilibrium conditions (see Sect. 3 for further details). The protolith is modeled by a simplified harzburgite bulk composition representative of the serpentinized Semail Ophiolite mantle section (OM94-52h; Hanghøj et al., 2010) in the FeO–$Fe_2O_3$–MgO–$SiO_2$ (FMS) + fluid system. To account for its initially variable $Fe^{3+}$ / $Fe_{TOT}$ due to serpentinization (Mayhew et al., 2018), the $Fe^{3+}$ / $Fe_{TOT}$-$XCO_2$ pseudosections are calculated (Fig. 7a) with (i) binary compositional mixing from reduced to fully oxidized and (ii) $H_2O$ and $CO_2$ considered saturated fluid phases. Serpentine is modeled by antigorite (Atg). Reaction products include magnesite, quartz, serpentine, talc, magnetite and hematite depending on $XCO_2$ ($CO_2$ / ($CO_2$ + $H_2O$) molar ratio) and $Fe^{3+}$ / $Fe_{TOT}$ (Fig. 7). Figure 7 illustrates the results obtained at constant pressure ($P$) and temperature ($T$) conditions of 0.3 GPa and 200 °C respectively.

Two endmember reaction pathways producing either Fe-rich or Mg-rich magnesites are identified: (A) at constant bulk $Fe^{3+}$ / $Fe_{TOT}$ and constant redox budget, increasing $XCO_2$ produces a change in phase assemblage and magnesite abundance, with magnetite reacting with $CO_2$ to form, first, $Fe^{2+}$-bearing magnesite and hematite and then Mg-rich magnesite; (B) change in the bulk redox budget with increasing (oxidation) or decreasing (reduction) $Fe^{3+}$ / $Fe_{TOT}$.

Representative of case A, the evolution of XMg in magnesite with increasing $XCO_2$ for a fixed bulk rock $Fe^{3+}$ / $Fe_{TOT}$ of 0.5 is shown in Fig. 7b. The high Fe content of magnesite is predicted in the Atg–Mgs–Hem stability field (XMg = 0.7), which is primarily a consequence of disappearing magnetite as $XCO_2$ increases. At high $XCO_2$, the model predicts Mg-rich magnesite compositions despite a lack of other silicate phases that incorporate iron because Fe is diluted within >65 % mol % of magnesite in the magnesite–quartz–hematite assemblage (Fig. 7b). Hence, the Fe redistribution during magnetite breakdown and the increasing magnesite abundance is likely to produce compositional zoning with progressive carbonation, even in a system at equilibrium. Predicted changes in XMg in magnesite between differently carbonated assemblages (corresponding to different

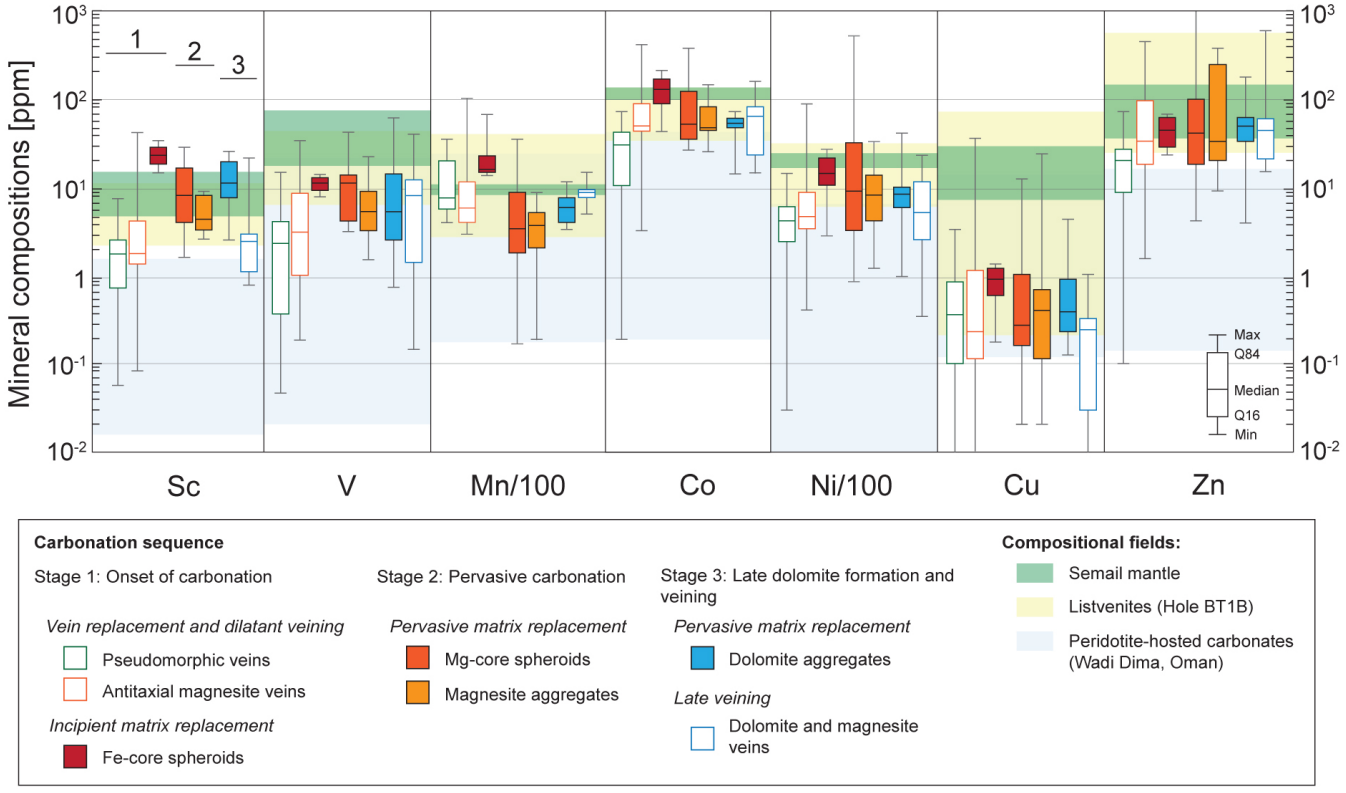


**Figure 6.** Caltech diagrams of the carbonate compositions in transition metals plotted on a log scale. The compositions of BT1B listvenites and the Semail mantle (data from Godard et al., 2021) and hydrothermal carbonates in the Semail Ophiolite (data from Noël et al., 2018) are represented by the colored background fields.

$XCO_2$) vary in their intensity depending on the bulk rock $Fe^{3+}$ / $Fe_{TOT}$, with only small changes in magnesite XMg in very oxidized compositions (Fig. 7a).

XMg isopleths are horizontal in most stability fields, and changes in the bulk redox budget (e.g., induced by the addition of reduced or oxidized fluids) will result in variations in magnesite composition (case B in Fig. 7a). The model predicts decreasing XMg of magnesite when the bulk $Fe^{3+}$ / $Fe_{TOT}$ decreases. This effect is the most pronounced at low-$XCO_2$ conditions, when serpentine is stable and magnesite abundance comparatively low. Interestingly, at these conditions, the complete transformation of magnetite to hematite and Fe-bearing magnesite is predicted to occur with relatively minor magnesite precipitation, independently of the initial bulk $Fe^{3+}$ / $Fe_{TOT}$.

Caveats arise when using thermodynamic modeling to interpret microstructural observations and geochemical analyses of highly reactive systems such as the Fanja listvenite series. It is important to note that fluid $XCO_2$ in Fig. 7 is not equivalent to the $CO_2$ concentration of the infiltrating fluid but to the $XCO_2$ that this fluid would acquire once equilibrated with the calculated mineral assemblages. Hence the model is applicable when the infiltrating $CO_2$-bearing fluids can be considered locally buffered to the $XCO_2$ corresponding to the equilibrium assemblage. It is not applicable if fluid fluxes are high and $CO_2$ renewal fast: the buffering capacity of the local mineral assemblage can then be kinetically overstepped, and reactions will become controlled predominantly by the infiltrating fluid composition.

## 5 Discussion

### 5.1 From serpentinite to listvenite: a stepwise carbonation sequence

The conversion of serpentinites to listvenites in the Fanja region produced a wealth of vein microstructures and matrix replacement textures including zoned magnesites of highly variable compositions. The abundant veins characterizing our samples indicate efficient cracking and faulting that favored, in turn, the recurrent redistribution of fluid pathways and the infiltration of highly reactive fluids throughout the identified sequences of carbonation (e.g., Kelemen et al., 2022; Menzel et al., 2022) despite the increase in rock volume associated with the formation of listvenites (e.g., Falk and Kelemen, 2015; Godard et al., 2021; Okazaki et al., 2021). Veins form a multi-scale discrete network with matrix replacement textures occurring as small (up to 1 mm) mag-

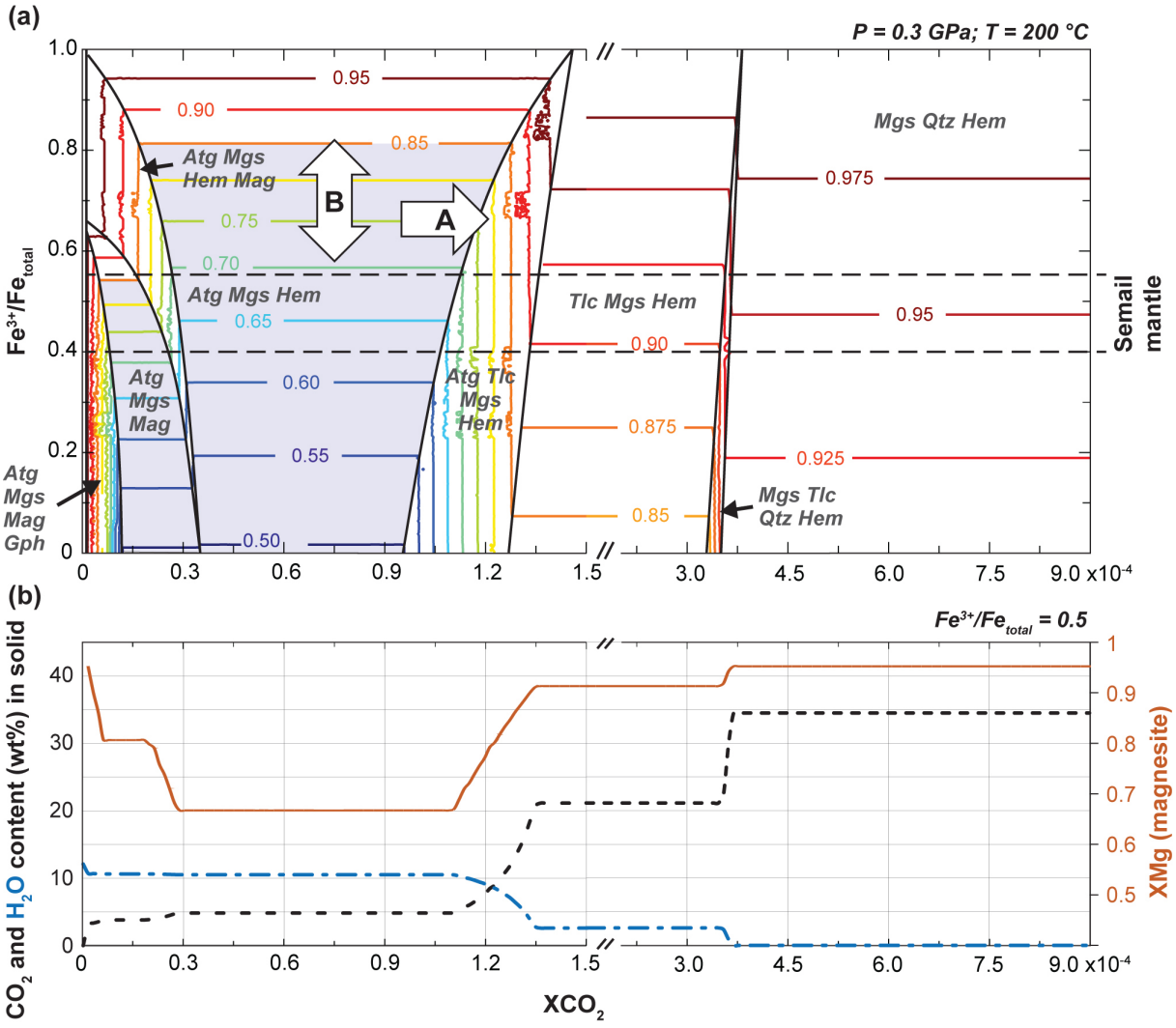


**Figure 7.** Model of Fe-partitioning in relation to carbonation and bulk rock redox budget. **(a)** Isobaric and isothermal, fluid-saturated $XCO_2$ pseudosection for a harzburgite bulk rock composition, with the y axis showing the redox budget expressed as $Fe^{3+}$ / $Fe_{TOT}$ (note that only in the small field at very low $XCO_2$ where graphite is predicted does the redox budget not directly equal $Fe^{3+}$ / $Fe_{TOT}$ here). Predicted XMg compositions of magnesite are shown as colored isopleths. **(b)** Plot of XMg of magnesite and $CO_2$ and $H_2O$ content in solid assemblage at a fixed redox budget of $Fe^{3+}$ / $Fe_{TOT} = 0.5$, illustrating the expected changes in magnesite composition for the case of redox-neutral carbonation. Modeling was done using a simplified hydrated harzburgite composition with binary compositional mixing from reduced ($SiO_2$ – 38.77 wt %; MgO – 39.21 wt %; FeO – 6.99 wt %) to fully oxidized ($SiO_2$ – 38.77 wt %; MgO – 39.21 wt %; $Fe_2O_3$ – 7.77 wt %) with saturated $H_2O$ and $CO_2$. For illustration purposes the results of two calculations at the same conditions but different ranges of $XCO_2$ were combined (note the change in scaling of the *x* axis). Blue fields are for Fe-rich magnesite compositions (XMg < 0.85). The following mineral abbreviations are used. Atg: antigorite; Gph: graphite, Hem: hematite, Mag: magnetite, Mgs: magnesite, Qz: quartz, Tlc: talc.

nesite, or more rarely dolomite, overgrowths to aggregates around the finest veins (e.g., Figs. 3b, S3, S4). Such a discrete and recurrent (re-)organization of fluid pathways favored the development of isolated micro-domains, with matrix replacement reactions more likely to occur at rock-dominated conditions. It also allowed the texture and composition of mineral assemblages formed during the earliest stages of the carbonation sequence in domains poorly or not affected by fracturation and faulting during the later stages of listvenite formation to be preserved.

Our investigations indicate that the early stages of carbonation proceeded as two main steps characterized by the formation of magnesite spheroids with (i) Fe-rich cores during incipient carbonation (Stage 1) and (ii) Mg-rich cores and Fe-rich rims during extended carbonation (Stage 2). Both types are observed in carbonated serpentinites and listvenites (Figs. 5 and S5), and we posit that they represent a type

feature of the carbonation sequence. This interpretation is in contrast however to models describing the formation of magnesite as resulting from single-step carbonation reactions after serpentine (Reaction R1) or talc (Reaction R2) (e.g., Johannes, 1969):

$$\begin{aligned}(Mg,Fe)_3Si_2O_5(OH)_4 + 3CO_{2\,aq} &= 3(Mg,Fe)CO_3 \\ &\quad + 2SiO_2 + 2H_2O \\ \text{Serpentine} + CO_{2\,aq} &= \text{Magnesite} \\ &\quad + \text{Quartz} + H_2O, \qquad \text{(R1)}\end{aligned}$$

or

$$\begin{aligned}(Mg,Fe)_3Si_4O_{10}(OH)_2 + 3CO_{2\,aq} &= 3(Mg,Fe)CO_3 \\ &\quad + 4SiO_2 + 2H_2O \\ \text{Talc} + CO_{2\,aq} &= \text{Magnesite} \\ &\quad + \text{Quartz} + H_2O. \qquad \text{(R2)}\end{aligned}$$

The Mg-rich magnesite spheroids, aggregates and overgrowths represent the most voluminous fraction of the matrix carbonates in the Fanja listvenites ($\sim$ 55 vol %; e.g., Fig. 5c). Mg-rich magnesites generally have subhedral to euhedral morphologies, suggesting formation at near-equilibrium conditions (Beinlich et al., 2020). This assumption is consistent with the geochemical analyses and maps of Mg-rich magnesites showing homogeneous chemical compositions at the millimeter-scale for (i) Mg-rich overgrowths around Fe-rich-core magnesites (Stage 1) and (ii) in the Mg-rich-core regions of spheroids and aggregates (Stage 2) (Fig. 5b and d). Thermodynamic modeling predicts the formation of high-XMg magnesite in the Tlc–Qz–Hem and in the Mgs–Qz–Hem stability fields (Fig. 7a), and the most favorable conditions are (i) a serpentinized protolith ($Fe^{3+}$ / $Fe_{TOT}$ > 0.6) and (ii) high-$XCO_2$ fluids ($> 1.3 \times 10^{-4}$). The bulk $Fe^{3+}$ / $Fe_{TOT}$ of the main mantle section of the Semail Ophiolite is typically 0.4–0.55 (Mayhew et al., 2018) and therefore too low to account for the Mg-rich compositions of the Fanja magnesites (XMg: $\sim$ 0.96), except after equilibration with high-$XCO_2$ fluids in the Mgs–Qz–Hem stability field. It should be noted that the stability domain of this mineral assemblage increases as temperatures decrease, and thus the formation of high-XMg magnesite should be facilitated during ophiolite cooling, even when considering constant chemical and redox conditions.

Fe-rich magnesite is widespread in the studied samples, although it represents only a minor fraction of the matrix carbonates ($\sim$ 8 vol %–19 vol %; e.g., Fig. 5; Table S12). It occurs as (i) Fe-core spheroids, typical of Stage 1 features, and (ii) thin rims around Mg-rich spheroids. Fe-rich magnesite is not uncommon in carbonated peridotites and listvenites where it occurs as Fe-rich zoning toward the rims of euhedral magnesites (e.g., Tominaga et al., 2017) or as Fe-rich overgrowth around Mg-rich magnesite (e.g., Menzel et al., 2018). Its formation is then ascribed to the complete dissolution of magnetite at high $XCO_2$ when stabilizing the Mgs + Qz assemblage and/or to precipitation in the presence of talc (Fig. 7a; Menzel et al., 2018). The textures and compositions of the Fanja Fe-rich magnesites however differ from previously studied samples: (i) all samples have magnesite compositions that are too high in Fe (XMg < 0.80) to be accounted for solely by fluid–rock equilibration in the presence of talc (XMg > 0.85; Fig. 7; Menzel et al., 2018; Sieber et al., 2022), (ii) the development of Fe-rich rims of Mg-core spheroids is associated with a change in magnesite texture from euhedral and anhedral to dendritic textures, suggesting changes in growth conditions (Fig. 5d), and (iii) Fe-core anhedral magnesite is often observed as coronae around Fe oxides (Fig. 4), a texture described here for the first time in listvenites. These characteristics suggest that the Fanja Fe-rich magnesites result from different reaction pathways in contrast to previously studied carbonated serpentinites and listvenites.

### 5.2 Origins of two Fe-enrichment trends in the Fanja magnesites

The differences in the textures of the Fe-rich magnesites can provide insights into their growth conditions and thus the possible origins of the two distinct types of Fe-enrichment observed in the Fanja magnesites.

Fe-rich-core magnesite and associated aggregates have anhedral to subhedral textures suggesting precipitation at or near equilibrium conditions. Based on this assumption, the very low XMg ($\sim$ 0.55–0.70) of Fe-rich-core magnesites and their volume fraction (e.g., 8 % in sample 50Z-1-75-80; Fig. 5a) can be interpreted as showing equilibration in the serpentine stability field between low-$XCO_2$ fluids and a typical Semail serpentinized peridotite (initial bulk $Fe^{3+}$ / $Fe_{TOT}$ $\sim$ 0.4–0.55; Mayhew et al., 2018; Fig. 8). The Fe-rich magnesite spheroids and aggregates are typically localized in the vicinity of Stage 1 serpentine and Fe-rich magnesite veins, suggesting that precursor serpentine veins and early carbonate veins acted as fluid pathways for these low-$XCO_2$ fluids during incipient carbonation. This hypothesis is supported by the high nanoporosity of the serpentine veins in comparison to nearby mesh lizardite (Menzel et al., 2022). In this context, the variations in the Fe composition of magnesite cores and aggregates from one sample to the other are attributed to changes in (i) the degree of serpentinization of the peridotite protolith (initial bulk $Fe^{3+}$ / $Fe_{TOT}$) and/or (ii) the oxygen fugacity of the low-$XCO_2$ infiltrating fluids (oxidized to reduced fluids) (Fig. 7a and b). This interpretation however overlooks the possible impact of the partial to complete dissolution of Fe oxides on Fe redistribution, redox changes and the role of fluid compositions (pH, ionic strength, ligands, etc.). Fe-core spheroids preserve textures showing the growth of anhedral magnesite at the expense of magnetite in several of the carbonated serpentinite (Fig. 4a) and listvenite (Fig. 4c) samples. Some samples also preserve microporous reaction zones with tiny hematite grains, outlining re-

licts of dissolving magnetite (Fig. 4c). The destabilization of magnetite in the presence of $CO_2$-rich fluids to form Fe-rich magnesite (siderite as $FeCO_3$) is written as follows (Frost, 1985):

$$(Fe^{2+}Fe_2^{3+})O_4 + 3CO_{2\,aq} = 3Fe^{2+}CO_3 + 0.5O_{2\,aq}$$
$$\text{Magnetite} + CO_{2\,aq} = \text{Siderite} + O_{2\,aq}. \quad \text{(R3)}$$

Reaction (R3) predicts an increase in oxygen fugacity; however, $O_{2\,(aq)}$ solubility is negligible in hydrothermal aqueous fluids in the range of $P$–$T$ conditions estimated for the formation of the Fanja listvenites. Therefore, it must be buffered by an oxidation reaction involving either infiltrating fluids and/or reacting minerals. Reaction (R3) could proceed through the oxidation of reduced fluid species (e.g., serpentinization-derived $H_2$), if present, to $CO_2$, carbonate and/or water. Alternatively, oxidation of magnetite is suggested by the presence of hematite around destabilized magnetite, and, assuming constant redox conditions, the formation of Fe-rich magnesite at the expense of magnetite can then be rewritten as

$$(Fe^{2+}Fe_2^{3+})O_4 + CO_{2\,aq} = Fe^{2+}CO_3 + Fe_2^{3+}O_3$$
$$\text{Magnetite} + CO_{2\,aq} = \text{Siderite} + \text{Hematite}. \quad \text{(R4)}$$

However, the transformation of magnetite into hematite could also reveal interactions with low-pH fluids rather than an oxidation reaction (Ohmoto, 2003; Zhao et al., 2010):

$$Fe_3O_4 + 2H_{aq}^{+} = Fe_2O_3 + Fe_{aq}^{2+} + H_2O$$
$$\text{Magnetite} + 2H_{aq}^{+} = \text{Hematite} + Fe_{aq}^{2+} + H_2O, \quad \text{(R5)}$$

with $Fe^{2+}$ precipitating as Fe-rich magnesite when dissolved $CO_2$ is present. The solubility of magnetite and the transport of $Fe^{2+}$ would also be enhanced in saline fluids rich in ligands ($CH_3COO^-$, $Cl^-$, ...; e.g., Zhao et al., 2010).

Our observations do not allow discriminating unquestionably these different reaction pathways for the formation of the Fe-core spheroids. The body of evidence suggesting that Fe-core spheroids form in low flow zones at an early stage of carbonation of the serpentinized precursor leads us however to opt for a coupled redox process (involving reduced fluids and/or solely Reaction R4) as the most likely reaction pathway for their formation. Nevertheless, the migration of low-pH and/or saline fluids likely represents an important vector for the remobilization of Fe, in particular for the Fe-rich rims of Mg-rich magnesite spheroids.

In contrast to Fe-core spheroids and aggregates, Fe-rich rims and associated outer cores of the Mg-rich magnesite spheroids are distinguished by their heterogeneities in textures and compositions: (i) the outer cores have euhedral to subhedral textures but contain abundant micro- to nanoscale quartz inclusions (Figs. 5d and S6j), (ii) they are also characterized by strong variations in compositions (Si, Ca, Mn; e.g., Figs. S5–S6, Tables S10–S11), and (iii) the Fe-rich rims have dendritic textures indicating fast growth kinetics. These variations suggest a departure from equilibrium conditions from cores to rims as the formation of the Mg-rich-core spheroids progressed. Another characteristic of the domains where high-Mg-core spheroids dominate is the lack of Fe-bearing oxides (magnetite, Cr-spinel) except for the occurrence of small hematite grains in the outer cores and in the background quartz matrix. In contrast to what is observed in Fe-core spheroids, these hematite grains sometimes have dissolution features, suggesting a change in reaction conditions during the formation of the Mg-core spheroids leading to disequilibrium conditions relative to the Mgs–Qz–Hem assemblage. Decreasing temperatures would increase the stability domain for these minerals, so we posit that these contrasting trends result primarily from changes in fluid composition with reacting fluids as carbonation progresses. These variations could result from (1) less efficient fluid renewal at the growing magnesite interface: carbonation reactions are typically associated with significant increases in volume (Kelemen et al., 2022), thus clogging fluid pathways (e.g., Andreani et al., 2009) and inducing, in turn, local changes in fluid composition and reaction pathways (e.g., Peuble et al., 2015a, b), and/or (2) changes in the composition of the inlet fluids as discussed for Fe-rich spheroids.

### 5.3 Interplays between carbonation reactions and fluid flow: consequences for trace metal redistribution

The dissolution of serpentinized peridotites during listvenite formation releases trace elements that will be either leached out of the reaction zones by the fluids to precipitate downstream or trapped locally by secondary minerals. The study of Hole BT1B listvenites and carbonated serpentinites shows that they have highly variable trace element bulk rock compositions compared to their serpentinized precursors, in particular for siderophile and chalcophile transition elements, even though mass balance calculations indicate that there is no fluid addition or loss for these elements at the scale of the borehole (Godard et al., 2021). Most trace elements being highly incompatible in quartz, carbonates represent, in volume, the major trapping mineral in listvenites. They overlap in composition with the bulk rock composition of the BT1B listvenites series, indicating that, except for Cu, they also account for a large part of their transition element budget (Fig. 6). These relatively rich compositions distinguish the Fanja carbonates from the hydrothermal carbonates from the Semail mantle section that are commonly depleted relative to the reacting host serpentinized peridotites (Noël et al., 2018). The Fanja carbonates have extremely variable compositions, beyond the range of the Hole BT1B listvenite series, yet different trends can be distinguished between vein and matrix carbonates and, to a lesser extent, between the three carbonation stages, giving insights into the respective roles of dissolution–precipitation reactions and transport in the redistribution of transition elements during carbonation.

Matrix carbonates have on average slightly higher concentrations compared to veins, Sc showing the most systematic differences between matrix and vein compositions. These differences are related in part to the large LA-ICP-MS spot size (100 µm) compared to that of carbonate minerals, particularly those forming spheroids and aggregates: matrix carbonate measurements are likely to include the contribution of the small magnetite and hematite grains typically associated with magnesite spheroids (Fig. 4), in particular in the small Fe-core spheroids. Nevertheless, they indicate also that most transition elements released by the dissolution of primary minerals will be trapped locally in carbonate and oxides when matrix carbonation occurs, in particular during the earliest stages of carbonation.

Only Mn shows significant differences in compositions from one stage of carbonation to the other for both vein and matrix carbonates: they are overall enriched in Stage 1 carbonates compared to Stage 2 and 3 carbonates. The mobility of Mn typically depends on redox conditions that are highly variable in the Fanja samples with, for example, bulk $Fe^{3+}$ / $Fe_{TOT}$ values of 0.13–0.61 in listvenites and 0.3–0.74 in carbonated serpentinites at Hole BT1B (Godard et al., 2021). The overlap between the compositions of the Semail serpentinized peridotites (Mayhew et al., 2018), the carbonated serpentinites and listvenites indicates that these variable redox values are not determined solely by changes in lithologies. Our mineralogical investigations show that, in addition to the complex sequences of dissolution and precipitation of oxides discussed previously, the conversion of serpentinites to carbonated serpentinites and listvenites is associated with the progressive disappearance of sulfides initially present in the protolith. Only rare carbonated serpentinites preserve Fe–Ni(–Co) sulfides (this study) or magnetite–awaruite assemblages (BT1B core; Beinlich et al., 2020) typically indicative of highly reducing conditions typical for serpentinization (Klein and Bach, 2009; de Obeso and Kelemen, 2020). On the other hand, the rare secondary Fe–Cu-rich sulfides observed in association with hematite in listvenites are indicative of oxidizing conditions, with oxygen fugacities several orders of magnitudes higher than for the magnetite–awaruite assemblages (Frost, 1985). The conversion of the magnetite and Fe–Ni sulfides to rare Fe–Cu-rich sulfides and abundant hematite in our samples points to a change to oxidizing conditions (Eckstrand, 1975; Frost, 1985). The lower Mn content of Stage 2 and 3 carbonates, predominant in listvenites, is likely related to the same process. On the same line, the scarcity or absence of sulfides in the Fanja samples may result from the oxidation of sulfide to highly soluble sulfate, as proposed for the fuchsite-bearing listvenites at the Gråberget ultramafic body (Austrheim et al., 2021). These reactions may participate in the mobilization of transition elements in fluids, especially for Cu and, to a lesser extent, Ni and Co: it could account for the depletion of carbonates in these elements compared to their serpentinized precursor. This suggests that transition elements having chalcophile affinity are the most likely to be leached out of reaction zones and act as fluid-mobile elements until conditions favorable for the precipitation of sulfide are reached in fluids (supersaturation, changes in carbon, sulfur or hydrogen speciation; e.g., Frost, 1985; Frost and Beard, 2007). Such a mechanism could account for the highly localized enrichments in these elements along BT1B cores (Godard et al., 2021) and the occurrence of small Cu veins observed in some listvenite samples (Kelemen et al., 2020) or in the field in Fanja. It is interesting to note that secondary sulfides are commonly observed in ore-bearing listvenites (e.g., Qiu and Zhu, 2018).

In contrast to most transition elements, there is no straightforward relationships between the overall distribution of V and Zn in carbonates, oxides and sulfides and their bulk rock compositions. V and Zn are concentrated in Cr-spinel, a mineral well preserved until the later stages of carbonation (Kelemen et al., 2020; Beinlich et al., 2020, this study), and they are enriched mostly in fuchsite (Tables S4, S10, S11). We posit that their complex distribution trends are related to their progressive release in fluids during the dissolution of Cr-spinel combined with a preferential trapping in fuchsite-rich zones (Godard et al., 2021).

## 6 Summary and conclusions

The petrological and chemical study of the Fanja listvenites and associated lithologies allows three stages of carbonation to be identified for the conversion of serpentinized peridotites to listvenites, with the development of replacive textures commonly observed at Stages 1 and 2, whilst carbonate (± quartz) veining becomes predominant in the later Stage 3. Carbonates are dominantly magnesite, but dolomite is also commonly observed at Stage 3. This study highlights also the widespread occurrence of Fe zoning in the matrix and vein magnesite developing during incipient carbonation. The pervasive replacement of serpentine by magnesite is characterized by the formation of spheroids, among which two types were identified based on the composition of their core regions: Mg-core and Fe-core spheroids. We also document for the first time in detail the different carbonation reactions destabilizing Fe oxides into Fe-rich magnesite, an essential mechanism to account for the development of Fe-core magnesites. Thermodynamic modeling converges on the precipitation of Fe-rich magnesite in equilibrium with serpentine at low fluid $XCO_2$ composition and variable local redox conditions. Fe-core spheroids characterize the onset of carbonation, followed by the pervasive (over-)growth of Mg-rich spheroids and aggregates at increasing fluid $XCO_2$ and/or during cooling. The relative scarcity of Fe-core spheroids compared to Mg-rich matrix magnesite may be a hint for a fast transition from limited to intensive fluxing of reactive fluid. This transition may be caused by the linkages between cyclic fluid pressure variations and brittle to cataclastic deformation under regional tectonic stress, related to reaction-

enhanced deformation (Menzel et al., 2022) and reaction-induced fracturing (e.g., Kelemen et al., 2022).

Carbonation triggers the destabilization of the minerals constituting serpentinized peridotites (silicates, minor oxides and sulfides), thereby influencing the redistribution of transition elements between minerals and fluids. In Fanja, carbonation to listvenite is accompanied by evolving assemblages of Fe oxides and sulfides. These implications have to be considered for mass transfers at a larger-scale, as listvenite formation is inferred to occur along basal sections of obducted ophiolites and in the shallow mantle wedge of subduction zones (Kelemen and Manning, 2015), with a potential impact on the cycling of metals.

*Data availability.* All data are contained in the figures of the paper and in the Supplement; raw images of these figures are available from the authors upon request. Data are available online on the EarthChem data repository: https://doi.org/10.26022/IEDA/112834 (Decrausaz et al., 2023).

*Sample availability.* Archive halves and samples of BT1B cores are available through the Oman Drilling Project (https://www.omandrilling.ac.uk/samples-data). Archive samples from Site 1 and Site 2 and all studied thin sections are stored at Géosciences Montpellier.

*Supplement.* The supplement related to this article is available online at: https://doi.org/10.5194/ejm-35-171-2023-supplement.

*Author contributions.* This work is part of TD's PhD thesis at Géosciences Montpellier. MG designed the project. TD, EO and RL conducted fieldwork. TD and EO refined geological maps. TD, MG, FP and MDM studied the petrography and the petrology. TD performed SEM imaging, EDX mapping, EPMA and LA-ICP-MS data acquisition and treatment, and image processing and drafted the figures. FB conducted EDS analyses. MDM performed thermodynamic modeling. All authors discussed and interpreted the results. TD and MG led the writing of the manuscript, to which all authors contributed.

*Competing interests.* The contact author has declared that none of the authors has any competing interests.

*Disclaimer.* Publisher's note: Copernicus Publications remains neutral with regard to jurisdictional claims in published maps and institutional affiliations.

*Acknowledgements.* We would like to thank Carla Tiraboschi and Jörg Hermann for their constructive reviews, as well as editor Reto Gieré, whose comments helped to improve several aspects of the paper. We thank Othmar Müntener, Martin Robyr, Alexey Ulianov and Olivier Reubi for allowing access to the laboratory facilities at the University of Lausanne during the COVID-19 pandemic and for their assistance during data acquisition. We also acknowledge Olivia Mauguin and Olivier Bruguier for their assistance at the Géosciences Montpellier laboratory facilities. This work benefited from constructive and appreciated discussions with Françoise Boudier. We thank the Sultanate of Oman Public Authority for Mining for support to conduct fieldwork and export samples. We also thank Sobhi Nasir for his support during the field trip in Oman.

This research used core samples provided by the Oman Drilling Project. The Oman Drilling Project (OmanDP) has been made possible through commingled funds from the International Continental Scientific Drilling Project (ICDP; Peter Kelemen, Jürg Matter, Damon Teagle lead PIs), the Sloan Foundation – Deep Carbon Observatory (grant 2014-3-01, Peter Kelemen PI), the National Science Foundation (NSF-EAR-1516300, Peter Kelemen lead PI), NASA – Astrobiology Institute (NNA15BB02A, Alexis Templeton PI), the German Research Foundation (DFG: KO 1723/21-1, Jürgen Koepke PI), the Japanese Society for the Promotion of Science (JSPS no. 16H06347, Katsuyoshi Michibayashi PI; and KAKENHI 16H02742, Eiichi Takazawa PI), the European Research Council (Adv: no. 669972; Bjorn Jamtveit PI), the Swiss National Science Foundation (SNF:20FI21_163073, Gretchen Früh-Green PI), JAMSTEC, the TAMU-JR Science Operator, and contributions from the Sultanate of Oman Ministry of Regional Municipalities and Water Resources, the Oman Public Authority of Mining, Sultan Qaboos University, CNRS-Univ. Montpellier, Columbia University of New York, and the University of Southampton.

*Financial support.* This research has been supported by the Agence Nationale de la Recherche (grant no. ANR-18-CE01-0014-01 LISZT), the German Research Foundation (grants nos. UR64/20-1 and UR 64/17-1) and the Junta de Andalucía (Consejeria de Conocimiento y Universidades) (postdoctoral fellowship grant no. Postdoc_21_00791).

*Review statement.* This paper was edited by Reto Gieré and reviewed by Carla Tiraboschi and Jörg Hermann.

## References

Aftabi, A. and Zarrinkoub, M. H.: Petrogeochemistry of listvenite association in metaophiolites of Sahlabad region, eastern Iran: Implications for possible epigenetic Cu–Au ore exploration in metaophiolites, Lithos, 156–159, 186–203, https://doi.org/10.1016/j.lithos.2012.11.006, 2013.

Alt, J. C., Schwarzenbach, E. M., Früh-Green, G. L., Shanks, W. C., Bernasconi, S. M., Garrido, C. J., Crispini, L., Gaggero, L., Padrón-Navarta, J. A., and Marchesi, C.: The role of serpentinites in cycling of carbon and sulfur: Seafloor serpentinization and subduction metamorphism, Lithos, 178, 40–54, https://doi.org/10.1016/j.lithos.2012.12.006, 2013.

Andreani, M., Luquot, L., Gouze, P., Godard, M., Hoisé, E., and Gibert, B.: Experimental Study of Carbon Sequestration Reactions Controlled by the Percolation of $CO_2$-Rich Brine

through Peridotites, Environ. Sci. Technol., 43, 1226–1231, https://doi.org/10.1021/es8018429, 2009.

Auclair, M., Gauthier, M., Trottier, J., Jebrak, M., and Chartrand, F.: Mineralogy, geochemistry, and paragenesis of the Eastern Metals serpentinite-associated Ni-Cu-Zn deposit, Quebec Appalachians, Econ. Geol., 88, 123–138, https://doi.org/10.2113/gsecongeo.88.1.123, 1993.

Austrheim, H., Corfu, F., and Renggli, C. J.: From peridotite to fuchsite bearing quartzite via carbonation and weathering: with implications for the Pb budget of continental crust, Contrib. Mineral. Petrol., 176, 94, https://doi.org/10.1007/s00410-021-01851-z, 2021.

Bechennec, F., Le Metour, J., Rabu, D., Bourdillon-de-Grissac, C., de Wever, P., Beurrier, M., and Villey, M.: The Hawasina Nappes: stratigraphy, palaeogeography and structural evolution of a fragment of the south-Tethyan passive continental margin, Geol. Soc. Spec. Publ., 49, 213–223, https://doi.org/10.1144/gsl.sp.1992.049.01.14, 1990.

Beinlich, A., Plümper, O., Hövelmann, J., Austrheim, H., and Jamtveit, B.: Massive serpentinite carbonation at Linnajavri, N–Norway, Terra Nova, 24, 446–455, https://doi.org/10.1111/j.1365-3121.2012.01083.x, 2012.

Beinlich, A., Plümper, O., Boter, E., Müller, I. A., Kourim, F., Ziegler, M., Harigane, Y., Lafay, R., Kelemen, P. B., and the Oman Drilling Project Science Team: Ultramafic rock carbonation: Constraints from listvenite core BT1B, Oman drilling project, J. Geophys. Res.-Sol. Ea., 125, e2019JB019060, https://doi.org/10.1029/2019JB019060, 2020.

Belogub, E. V., Melekestseva, I. Y., Novoselov, K. A., Zabotina, M. V., Tret'yakov, G. A., Zaykov, V. V., and Yuminov, A. M.: Listvenite-related gold deposits of the South Urals (Russia): A review, Ore Geol. Rev., 85, 247–270, https://doi.org/10.1016/j.oregeorev.2016.11.008, 2017.

Boskabadi, A., Pitcairn, I. K., Leybourne, M. I., Teagle, D. A. H., Cooper, M. J., Hadizadeh, H., Bezenjani, R. N., and Bagherzadeh, R. M.: Carbonation of ophiolitic ultramafic rocks: Listvenite formation in the Late Cretaceous ophiolites of eastern Iran, Lithos, 352/353, 105307, https://doi.org/10.1016/j.lithos.2019.105307, 2020.

Boudier, F. and Nicolas, A.: Synchronous Seafloor Spreading and Subduction at the Paleo-Convergent Margin of Semail and Arabia, Tectonics, 37, 2961–2982, https://doi.org/10.1029/2018TC005099, 2018.

Boudier, F., Ceuleneer, G., and Nicolas, A.: Shear zones, thrusts and related magmatism in the Oman ophiolite: Initiation of thrusting on an oceanic ridge, Tectonophysics, 151, 275–296, https://doi.org/10.1016/0040-1951(88)90249-1, 1988.

Boudier, F., Baronnet, A., and Mainprice, D.: Serpentine mineral replacements of natural olivine and their seismic implications: Oceanic lizardite versus subduction-related antigorite, J. Petrol., 51, 495–512, https://doi.org/10.1093/petrology/egp049, 2010.

Buisson, G. and Leblanc, M.: Gold in carbonatized ultramafic rocks from ophiolite complexes, Econ. Geol., 80, 2028–2029, https://doi.org/10.2113/gsecongeo.80.7.2028, 1985.

Cannaò, E., Scambelluri, M., Bebout, G. E., Agostini, S., Pettke, T., Godard, M., and Crispini, L.: Ophicarbonate evolution from seafloor to subduction and implications for deep-Earth C cycling, Chem. Geol., 546, 119626, https://doi.org/10.1016/j.chemgeo.2020.119626, 2020.

Coleman, R.: Tectonic setting for ophiolite obduction in Oman, J. Geophys. Res.-Sol. Ea., 86, 2497–2508, https://doi.org/10.1029/JB086iB04p02497, 1981.

Connolly, J. A. D.: Computation of phase equilibria by linear programming: A tool for geodynamic modeling and its application to subduction zone decarbonation, Earth Planet. Sc. Lett., 236, 524–541, https://doi.org/10.1016/j.epsl.2005.04.033, 2005.

Connolly, J. A. D.: The geodynamic equation of state: What and how, Geochem. Geophy. Geosy. 10, Q10014, https://doi.org/10.1029/2009GC002540, 2009.

Debret, B., Bouilhol, P., Pons, M. L., and Williams, H.: Carbonate Transfer during the Onset of Slab Devolatilization: New Insights from Fe and Zn Stable Isotopes, J. Petrol., 59, 1145–1166, https://doi.org/10.1093/petrology/egy057, 2018.

Decrausaz, T., Godard, M., Menzel, M.D., Parat, F., Oliot, E., Lafay, R., and Barou, F.: Major and trace element mineral compositions of carbonated serpentinites and listvenites from Oman Drilling Project Hole BT1B (Semail Ophiolite, Oman), Version 2.0, Interdisciplinary Earth Data Alliance (IEDA) [data set], https://doi.org/10.26022/IEDA/112834, 2023.

de Obeso J. C. and Kelemen, P. B.: Major element mobility during serpentinization, oxidation and weathering of mantle peridotite at low temperatures, Philos. T. R. Soc. A, 378, 20180433, https://doi.org/10.1098/rsta.2018.0433, 2020.

Deschamps, F., Godard, M., Guillot, S., and Hattori, K.: Geochemistry of subduction zone serpentinites: A review, Lithos, 178, 96–127, https://doi.org/10.1016/j.lithos.2013.05.019, 2013.

Eckstrand, O. R.: The Dumont serpentinite; a model for control of nickeliferous opaque mineral assemblages by alteration reactions in ultramafic rocks, Econ. Geol., 70, 183–201, https://doi.org/10.2113/gsecongeo.70.1.183, 1975.

Emam, A. and Zoheir, B.: Au and Cr mobilization through metasomatism: Microchemical evidence from ore-bearing listvenite, South Eastern Desert of Egypt, J. Geochem. Explor., 125, 34–45, https://doi.org/10.1016/j.gexplo.2012.11.004

Falk, E. S. and Kelemen P. B.: Geochemistry and petrology of listvenite in the Samail ophiolite, Sultanate of Oman: Complete carbonation of peridotite during ophiolite emplacement, Geochim. Cosmochim. Ac., 160, 70–90, https://doi.org/10.1016/j.gca.2015.03.014, 2015.

Frost, B. R.: On the Stability of Sulfides, Oxides, and Native Metals in Serpentinite, J. Petrol., 26, 31–63, https://doi.org/10.1093/petrology/26.1.31, 1985.

Frost, B. R. and Beard, J. S.: On Silica Activity and Serpentinization, J. Petrol., 48, 1351–1368, https://doi.org/10.1093/petrology/egm021, 2007.

Gahlan, H. A., Azer, M. K., Asimow, P. D., and Al-Kahtany, K. M.: Petrogenesis of gold-bearing listvenites from the carbonatized mantle section of the Neoproterozoic Ess ophiolite, Western Arabian Shield, Saudi Arabia, Lithos, 372–373, 105679, https://doi.org/10.1016/j.lithos.2020.105679, 2020.

Garber, J. M., Rioux, M., Searle, M. P., Kylander-Clark, A. R. C., Hacker, B. R., Vervoort, J. D., Warren, C. J., and Smye, A. J.: Dating continental subduction beneath the Samail Ophiolite: Garnet, zircon, and rutile petrochronology of the As Sifah eclogites, NE Oman. J. Geophys. Res.-Sol. Ea., 126, e2021JB022715, https://doi.org/10.1029/2021JB022715, 2021.

Glennie, K. W., Boeuf, M. G. A., Hugues Clark, M. W., Moody-Stuart, M., Pilaar, W. F. H., and Reinhardt, B. M.: Geology of the

Oman Mountains, Neder. Mijn. Geol. Genoot., Delft, the Netherlands, 423 pp., ISBN 978-90-01-01310-3, 1974.

Godard, M., Jousselin, D., and Bodinier, J.-L.: Relationships between geochemistry and structure beneath a paleo-spreading centre: a study of the mantle section in the Oman ophiolite, Earth Planet. Sc. Lett., 180, 133–148, https://doi.org/10.1016/S0012-821X(00)00149-7, 2000.

Godard, M., Carter, E. J., Decrausaz, T., Lafay, R., Bennett, E., Kourim, F., de Obeso, J. C., Michibayashi, K., Harris, M., Coggon, J., Teagle, D., Kelemen, P., and the Oman Drilling Project Phase 1 Science Party: Geochemical Profiles Across the Listvenite-Metamorphic Transition in the Basal Megathrust of the Semail Ophiolite: Results from Drilling at Oman DP Hole BT1B, J. Geophys. Res.-Sol. Ea., 126, e2021JB022733, https://doi.org/10.1029/2021JB022733, 2021.

Griffin, W., Powell, W., Pearson, N. J., and O'Reilly, S.: GLITTER: data reduction software for laser ablation ICP-MS, Short Course Series, 40, 308–311, 2008.

Halls, C. and Zhao, R.: Listvenite and related rocks: perspectives on terminology and mineralogy with reference to an occurrence at Cregganbaun, Co. Mayo, Republic of Ireland, Mineral. Deposita, 30, 303–313, https://doi.org/10.1007/BF00196366, 1995.

Hanghøj, K., Kelemen, P. B., Hassler, D., and Godard, M.: Composition and Genesis of Depleted Mantle Peridotites from the Wadi Tayin Massif, Oman Ophiolite; Major and Trace Element Geochemistry, and Os Isotope and PGE Systematics, J. Petrol., 51, 201–227, https://doi.org/10.1093/petrology/egp077, 2010.

Hansen, L. D., Dipple, G. M., Gordon, T. M., and Kellett, D. A.: Carbonated serpentinite (listwanite) at Atlin, British Columbia: a geological analogue to carbon dioxide sequestration, Can. Mineral., 43, 225–239, https://doi.org/10.2113/gscanmin.43.1.225, 2015.

Hinsken, T., Bröcker, M., Strauss, H., and Bulle, F.: Geochemical, isotopic and geochronological characterization of listvenite from the Upper Unit on Tinos, Cyclades, Greece, Lithos, 282/283, 281–297, https://doi.org/10.1016/j.lithos.2017.02.019, 2017.

Holland, T. and Powell, R.: An improved and extended internally consistent thermodynamic dataset for phases of petrological interest, involving a new equation of state for solids, J. Metamorph. Geol., 29, 333–383, https://doi.org/10.1111/j.1525-1314.2010.00923.x, 2011.

Holland, T. J. B. and Powell, R.: An internally consistent thermodynamic data set for phases of petrological interest, J. Metamorph. Geol., 16, 309–343, https://doi.org/10.1111/j.1525-1314.1998.00140.x, 1998.

Johannes, W.: An experimental investigation of the system $MgO$-$SiO_2$–$H_2O$-$CO_2$, Am. J. Sci., 267, 1083–1104, https://doi.org/10.2475/ajs.267.9.1083, 1969.

Kelemen, P. B. and Matter, J. M.: In situ carbonation of peridotite for CO2 storage, P. Natl. Acad. Sci. USA, 105, 17295–17300, https://doi.org/10.1073/pnas.0805794105, 2008.

Kelemen, P. B. and Manning, C. E.: Reevaluating carbon fluxes in subduction zones, what goes down, mostly comes up, P. Natl. Acad. Sci. USA, 112, 30, https://doi.org/10.1073/pnas.1507889112, 2015.

Kelemen, P. B., Matter, J. M., Teagle, D. A. H., Coggon, J. A., and the Oman Drilling Project Science Team: Site BT1: fluid and mass exchange on a subduction zone plate boundary, in: Proceedings of the Oman Drilling Project, College Station, Texas, International Ocean Discovery Program, International Ocean Discovery Program, https://doi.org/10.14379/OmanDP.proc.2020, 2020.

Kelemen, P. B., de Obeso, J. C., Leong, J. A., Godard, M., Okazaki, K., Kotowski, A. J., Manning, C. E., Ellison, E. T., Menzel, M. D., Urai, J. L., Hirth, G., Rioux, M., Stockli, D. F., Lafay, R., Beinlich, A. M., Coggon, J. A., Warsi, N. H., Matter, J. M., Teagle, D. A. H., Harris, M., Michibayashi, K., Takazawa, E., Al Sulaimani, Z., and the Oman Drilling Project Science Team: Listvenite formation during mass transfer into the leading edge of the mantle wedge: Initial results from Oman Drilling Project Hole BT1B, J. Geophys. Res.-Sol. Ea., 127, e2021JB022352, https://doi.org/10.1029/2021JB022352, 2022.

Khedr, M. Z., Arai, S., and Python, M.: Petrology and chemistry of basal lherzolites above the metamorphic sole from Wadi Sarami central Oman ophiolite, J. Mineral. Petrol. Sci., 108, 13–24, https://doi.org/10.2465/jmps.121026, 2013.

Klein, F. and Bach, W.: Fe-Ni-Co-O-S Phase Relations in Peridotite-Seawater Interactions, J. Petrol., 50, 37–59, https://doi.org/10.1093/petrology/egn071, 2009.

Lanari, P., Vho, A., Bovay, T., Airaghi, L., and Centrella, S.: Quantitative compositional mapping of mineral phases by electron probe micro-analyser, Geol. Soc. Spec. Publ., 478, 39–63, https://doi.org/10.1144/SP478.4, 2019.

Lippard, S. J., Shelton, A. W., and Gass, I. G.: The Ophiolite of Northern Oman, Geological Society of London Memoir 11, Blackwell Scientific Publications, Oxford, 178 pp., Blackwell Scientific Publications, ISBN 0 632 01587 X, 1986.

Mayhew, L. E., Ellison, E. T., Miller, H. M., Kelemen, P. B., and Templeton, A. S.: Iron transformations during low temperature alteration of variably serpentinized rocks from the Samail ophiolite, Oman, Geochim. Cosmochim. Ac., 222, 704–728, https://doi.org/10.1016/j.gca.2017.11.023, 2018.

Menzel, M. D., Garrido, C. J., Sánchez-Vizcaíno V. L., Marchesi, C., Hidas, K., Escayola, M. P., and Huertas, A. D.: Carbonation of mantle peridotite by $CO_2$-rich fluids: the formation of listvenites in the Advocate ophiolite complex (Newfoundland, Canada), Lithos, 323, 238–261, https://doi.org/10.1016/j.lithos.2018.06.001, 2018.

Menzel, M. D., Urai, J. L., de Obeso, J. C., Kotowski, A., Manning, C. E., Kelemen, P. B., Kettermann, M., Jesus, A. P., Harigane, Y., and the Oman Drilling Project Phase 1 Science Party: Brittle Deformation of Carbonated Peridotite-Insights From Listvenites of the Samail Ophiolite (Oman Drilling Project Hole BT1B), J. Geophys. Res.-Sol. Ea., 125, e2020JB020199, https://doi.org/10.1029/2020JB020199, 2020.

Menzel, M. D., Urai, J. L., Ukar, E., Decrausaz, T., and Godard, M.: Progressive veining during peridotite carbonation: insights from listvenites in Hole BT1B, Samail ophiolite (Oman), Solid Earth, 13, 1191–1218, https://doi.org/10.5194/se-13-1191-2022, 2022.

Nasir, S., Al Sayigh, A. R., Al Harthy, A., Al-Khirbash, S., Al-Jaaidi, O., Musllam, A., Al-Mishwat, A., and Al-Bu'saidi, S.: Mineralogical and geochemical characterization of listwaenite from the Semail Ophiolite, Oman, Geochemistry, 67, 213–228, https://doi.org/10.1016/j.chemer.2005.01.003, 2007.

Nicolas, A., Boudier, F., Ildefonse, I., and Ball, E.: Accretion of Oman and United Arab Emirates ophiolite – Discussion of a new structural map, Mar. Geophys. Res., 21, 147–180, https://doi.org/10.1023/A:1026769727917, 2000.

Noël, J., Godard, M., Oliot, E., Martinez, I., Williams, M., Boudier, F., Rodriguez, O., Chaduteau, C., Escario, S., and Gouze, P.: Evidence of polygenetic carbon trapping in the Oman Ophiolite: Petro-structural, geochemical, and carbon and oxygen isotope study of the Wadi Dima harzburgite-hosted carbonates (Wadi Tayin massif, Sultanate of Oman), Lithos, 323, 218–237, https://doi.org/10.1016/j.lithos.2018.08.020, 2018.

Okazaki, K., Michibayashi, K., Hatakeyama, K., Abe, N., Johnson, K. T. M., Kelemen, P. B., and the Oman Drilling Project Science Team: Major mineral fraction and physical properties of carbonated peridotite (listvenite) from ICDP Oman Drilling Project Hole BT1B inferred from X-ray CT core images, J. Geophys. Res.-Sol. Ea., 126, e2021JB022719, https://doi.org/10.1029/2021JB022719, 2021.

Oman Drilling Project: Samples & Data, Oman Drilling Project [data set], https://www.omandrilling.ac.uk/samples-data#SOAC, last access: 2 January 2023.

Padrón-Navarta, J. A., López Sánchez-Vizcaíno, V., Hermann, J., Connolly, J. A. D., Garrido, C. J., Gómez-Pugnaire, M. T., and Marchesi, C.: Tschermak's substitution in antigorite and consequences for phase relations and water liberation in high-grade serpentinites, Lithos, 178, 186–196, https://doi.org/10.1016/j.lithos.2013.02.001, 2013.

Peuble, S., Godard, M., Luquot, L., Andreani, M., Martinez, I., and Gouze, P.: $CO_2$ geological storage in olivine rich basaltic aquifers: New insights from reactive-percolation experiments, Appl. Geochem., 52, 174–190, https://doi.org/10.1016/j.apgeochem.2014.11.024, 2015a.

Peuble, S., Andreani, M., Godard, M., Gouze, P., Barou, F., Van De Moortele, B., Mainprice, D., and Reynard, B.: Carbonate mineralization in percolated olivine aggregates: Linking effects of crystallographic orientation and fluid flow, Am. Min., 100, 474–482, https://doi.org/10.2138/am-2015-4913, 2015b.

Pitzer, K. S. and Sterner, S. M.: Equations of state valid continuously from zero to extreme pressures with $H_2O$ and $CO_2$ as examples, Int. J. Thermophys., 16, 511–518, https://doi.org/10.1007/BF01441917, 1995.

Prigent, C., Agard, P., Guillot, S., Godard, M., and Dubacq, B.: Mantle wedge (de)formation during subduction infancy: evidence from the base of the Semail ophiolitic mantle, J. Petrol., 59, 2061–2091, 2018.

Qiu, T. and Zhu, Y.: Listwaenite in the Sartohay ophiolitic mélange (Xinjiang, China): A genetic model based on petrology, U-Pb chronology and trace element geochemistry, Lithos, 302/303, 427–446, https://doi.org/10.1016/j.lithos.2018.01.029, 2018.

Rioux, M., Garber, J. M., Searle, M., Kelemen, P. B., Miyashita, S., Adachi, Y., and Bowring, S.: High-Precision U-Pb Zircon Dating of Late Magmatism in the Samail Ophiolite: A Record of Subduction Initiation, J. Geophys. Res.-Sol. Ea., 126, e2020JB020758, https://doi.org/10.1029/2020JB020760, 2021.

Schröder, T., Bach, W., Jöns, N., Jöns, S., Monien, P., and Klügel, A.: Fluid circulation and carbonate vein precipitation in the footwall of an oceanic core complex, Ocean Drilling Program Site 175, Mid-Atlantic Ridge, Geochem. Geophy. Geosy., 16, 3716–3732, https://doi.org/10.1002/2015GC006041, 2015.

Schwarzenbach, E. M., Früh-Green, G. L., Bernasconi, S. M., Alt, J. C., and Plas, A.: Serpentinization and carbon sequestration: A study of two ancient peridotite-hosted hydrothermal systems, Chem. Geol., 351, 115–133, https://doi.org/10.1016/j.chemgeo.2013.05.016, 2013.

Searle, M. J. and Cox, J.: Tectonic setting, origin, and obduction of the Oman ophiolite, Geol. Soc. Am. Bull., 111, 104–122, https://doi.org/10.1130/0016-7606(1999)111<0104:TSOAOO>2.3.CO;2, 1999.

Sieber, M. J., Yaxley, G. M., and Hermann, J.: COH-fluid induced metasomatism of peridotites in the forearc mantle, Contrib. Mineral. Petrol., 177, 44, https://doi.org/10.1007/s00410-022-01905-w, 2022.

Soret, M., Agard, P., Dubacq, B., Plunder, A., and Yamato, P.: Petrological evidence for stepwise accretion of metamorphic soles during subduction infancy (Semail ophiolite, Oman and UAE), J. Metamorph. Geol., 35, 1051–1080, https://doi.org/10.1111/jmg.12267, 2017.

Stanger, G.: Silicified serpentinite in the Semail nappe of Oman, Lithos, 18, 13–22, https://doi.org/10.1016/0024-4937(85)90003-9, 1985.

Takazawa, E., Okayasu, T., and Satoh, K.: Geochemistry and origin of the basal lherzolites from the northern Oman ophiolite (northern Fizh block), Geochem. Geophy. Geosy., 4, 1021, https://doi.org/10.1029/2001GC000232, 2013.

Tominaga, M., Beinlich, A., Lima, E. A., Tivey, M. A., Hampton, B. A., Weiss, B., and Harigane, Y.: Multi-scale magnetic mapping of serpentinite carbonation, Nat. Commun., 8, 1870, https://doi.org/10.1038/s41467-017-01610-4, 2017.

Ulrich, M., Muñoz, M., Guillot, S., Cathelineau, M., Picard, C., Quesnel, B., Boulvais, P., and Couteau, C.: Dissolution-precipitation processes governing the carbonation and silicification of the serpentinite sole of the New Caledonia ophiolite, Contrib. Mineral. Petrol., 167, 952, https://doi.org/10.1007/s00410-013-0952-8, 2014.

Villey, M., Le Metour, J., and De Gramont, X.: Geological map of Fanja, Sheet NF 40-3F, Explanatory Notes, BRGM and Oman Ministry of Petroleum and Minerals, Oman Ministry of Petroleum and Minerals, 1986.

Wilde, A., Simpson, L., and Hanna, S., Preliminary study of Cenozoic hydrothermal alteration and platinum deposition in the Oman Ophiolite, J. Virtual Explor., 6, 7–13, 2002.

Zhao, J., Brugger, J., and Pring, A.: Mechanism and kinetics of hydrothermal replacement of magnetite by hematite, Geosci. Front., 10, 29–41, https://doi.org/10.1016/j.gsf.2018.05.015, 2010.